molecules

MDPI

Article

Deposition of Tetracoordinate Co(II) Complex with Chalcone Ligands on Graphene

Jakub Hrubý [1], Šárka Vavrečková [1,2], Lukáš Masaryk [3], Antonín Sojka [1], Jorge Navarro-Giraldo [1], Miroslav Bartoš [1], Radovan Herchel [3], Ján Moncol [4], Ivan Nemec [1,3] and Petr Neugebauer [1,*]

1 Central European Institute of Technology, CEITEC BUT, Purkyňova 656/123, 61200 Brno, Czech Republic; Jakub.Hruby@ceitec.vutbr.cz (J.H.); 200777@vutbr.cz (S.V.); Antonin.Sojka@ceitec.vutbr.cz (A.S.); Jorge.Navarro@ceitec.vutbr.cz (J.N.-G.); Miroslav.Bartos@ceitec.vutbr.cz (M.B.); Ivan.Nemec@ceitec.vutbr.cz (I.N.)

2 Institute of Physical Engineering, Faculty of Mechanical Engineering, Brno University of Technology, Technická 2, 61669 Brno, Czech Republic

3 Department of Inorganic Chemistry, Faculty of Science, Palacký University, 17. listopadu 12, 77147 Olomouc, Czech Republic; lukas.masaryk01@upol.cz (L.M.); radovan.herchel@upol.cz (R.H.)

4 Department of Inorganic Chemistry, Faculty of Chemical and Food Technology, Slovak University of Technology in Bratislava, 81237 Bratislava, Slovakia; jan.moncol@stuba.sk

* Correspondence: petr.neugebauer@ceitec.vutbr.cz; Tel.: +42-054-114-9727

Academic Editor: Daniela Meroni

Received: 6 October 2020; Accepted: 28 October 2020; Published: 29 October 2020

Abstract: Studying the properties of complex molecules on surfaces is still mostly an unexplored research area because the deposition of the metal complexes has many pitfalls. Herein, we probed the possibility to produce surface hybrids by depositing a Co(II)-based complex with chalcone ligands on chemical vapor deposition (CVD)-grown graphene by a wet-chemistry approach and by thermal sublimation under high vacuum. Samples were characterized by high-frequency electron spin resonance (HF-ESR), XPS, Raman spectroscopy, atomic force microscopy (AFM), and optical microscopy, supported with density functional theory (DFT) and complete active space self-consistent field (CASSCF)/N-electron valence second-order perturbation theory (NEVPT2) calculations. This compound's rationale is its structure, with several aromatic rings for weak binding and possible favorable π–π stacking onto graphene. In contrast to expectations, we observed the formation of nanodroplets on graphene for a drop-cast sample and microcrystallites localized at grain boundaries and defects after thermal sublimation.

Keywords: graphene; cobalt complexes; hybrid material; magneto-chemistry

1. Introduction

Nearly three decades have already passed since the first description of the slow relaxation of magnetization in the polynuclear cluster $[Mn_{12}O_{12}(O_2CCH_3)_{16}(H_2O)_4]$ known as Mn_{12} [1–3], which started the whole new research field of molecular magnetism [4]. These so-called Single-Molecule Magnets (SMMs) exhibit magnetic bistability up to a specific blocking temperature manifested by an intrinsic spin-reversal barrier energy (U_{eff}). The barrier is a function of the total spin in the ground state (S) and the axial component of magnetic dipole–dipole interaction (D) as follows: $U_{\text{eff}} = |D| \times S^2$ for integer spins and $U_{\text{eff}} = |D| \times \left(S^2 - \frac{1}{4}\right)$ for non-integer spins, respectively, in axial symmetry. This alone would imply that by increasing the number of magnetic centers, a better SMM would be obtained; however, there is a dependency of $D \propto \frac{1}{S^2}$ that stems from spin-orbit contributions to the D-tensor [5]. This dependency shifted the interest from rather large molecules with many magnetic

atoms to Single-Ion Magnets (SIMs) [6]. Several challenges need to be addressed before fully utilizing these SIMs in real applications. One of the challenges is increasing the blocking temperature, which was recently found to be 80 K in dysprosium metallocene in 2018 [7]. This temperature, above the boiling point of liquid nitrogen (77 K), already holds promise for possible applications in spintronics [8], quantum computing [9], and molecular electronics [10]. The second challenge is finding the way from bulk material to functional surfaces.

The magnetic properties of magnetic molecules can be precisely measured by high-frequency electron spin resonance (HF-ESR) both in bulk [11–20] and on a surface [21–23]. Primarily, the Zeeman and zero-field-splitting (ZFS) contributions to the spin Hamiltonian with information about the intrinsic magnetic properties of a molecule can be determined. Today, the current effort is focused on making thin films, ordered arrays, or self-assembled monolayers that will lead to technological applications [24,25]. The key for this is to understand the behavior and adsorption of complex molecules on surfaces since their exposed surface offers many application possibilities but also brings many challenges, as these molecules can oxidize, decompose, or degrade in ambient conditions. There are two main ways to produce nanostructured magnetic thin films. They can be deposited onto a substrate via a wet-chemistry protocol from a solution [26–28] or by thermal sublimation in vacuum [29–34].

The electrical addressing of SMMs can be provided via a conductive substrate. A promising candidate is an atomically thin layer of graphite, known as graphene [35], which is an interesting substrate due to its high electron mobility [36,37], mechanical strength [38], and thermal conductivity [39]. The original preparation technique firstly used to prepare graphene in 2004 was micro-mechanical cleavage [40]. This method is suitable for tens-of-micrometers-large flakes; however, more industrial techniques for large and homogeneous surface coverage soon emerged, such as graphene production by chemical vapor deposition (CVD) [41], on silicon carbide [42], by liquid-phase exfoliation [43], or by large-scale roll-to-roll printing [44]. The perfect graphene is a zero-gap semiconductor, which helps the charge carrier mobility but also limits the applications.

Herein, we report on the synthesis, crystal structure, magnetic properties, and characterization of a new tetracoordinate complex $[Co(4MeO\text{-}L)_2Cl_2]$ (**1**) with the chalcone imidazole-derivative ligand 4MeO-L = (2E)-3-[4-(1H-imidazol-1-yl)phenyl]-1-(4-methoxyphenyl)prop-2-en-1-on. The determination of the crystal structure revealed that this compound is tetracoordinate, and its molecules possess a unique shape with a large angle between the coordinated 4MeO-L ligands (vide infra). Tetracoordinate Co(II) compounds very often exhibit large easy-axis ($D < 0$) or easy-plane ($D > 0$) magnetic anisotropies [45]. Furthermore, the "flat" molecular shape involving the large aromatic system of the ligands might help to anchor complex molecules on surfaces such as graphene by non-covalent interactions. Therefore, we decided to thoroughly characterize the electronic structure of **1** by HF-ESR, to investigate both wet-chemistry and thermal sublimation depositions, and, thus, to produce a hybrid material composed of highly anisotropic Co(II)-based molecules and graphene. These samples were then characterized by Raman spectroscopy, X-ray photoelectron spectroscopy (XPS), and atomic force microscopy (AFM).

2. Results and Discussion

2.1. Synthesis and Crystal Structure of ***1***

The chalcone ligand 4MeO-L was prepared by the aldol condensation of 4'-(imidazol-1-yl)benzaldehyde with 4-methoxyacetophenone, as is shown in Scheme 1. The purity and structure of 4MeO-L were confirmed by ^{1}H and ^{13}C NMR spectroscopy, mass spectrometry, and elemental analysis. The complex **1** was synthesized by a reaction between $CoCl_2 \cdot 6H_2O$ and 4MeO-L (molar ratio, 1:2) in methanolic solution, and it precipitated as a blue microcrystalline powder. Recrystallization from methanol led to the isolation of pale blue crystals suitable for single-crystal diffraction. The purity of **1** was confirmed by elemental analysis, and the phase purity, by powder diffraction experiments.

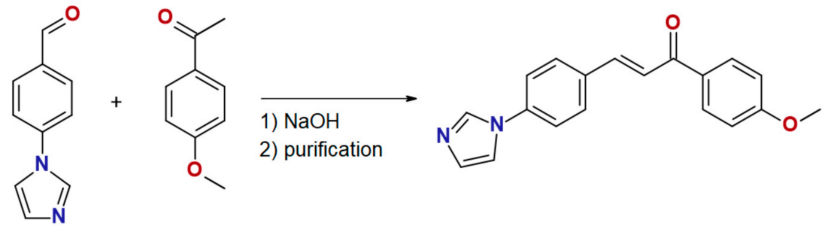

Scheme 1. Preparation of ligand 4MeO-L.

Compound **1** crystallizes in the monoclinic space group *Pc*, and it consists of tetracoordinate $[Co(4MeO\text{-}L)_2Cl_2]$ molecules (Figure 1). The 4MeO-L ligands coordinate to the Co atom by the imidazolyl nitrogen atoms forming the Co-N bonds (*d*(Co-N) = 2.014(4) and 2.016(4) Å), while the chlorido ligands form longer bonds (*d*(Co-Cl) = 2.255(2) and 2.257(2) Å). The overall shape of the coordination polyhedron can be described best as a significantly distorted tetrahedron adopting C_{2v} pseudosymmetry (continuous shape measures index [46,47] for T_d: 1.356 in **1**). The 4MeO-L ligands adopt an *E* conformation and remain planar even after coordination (Figure 1). The N-Co-N angle is wider than the Cl-Co-Cl one: <(N1-Co1-N2) = 125.7(2) vs. <(Cl1-Co1-Cl2) = 119.44(6).

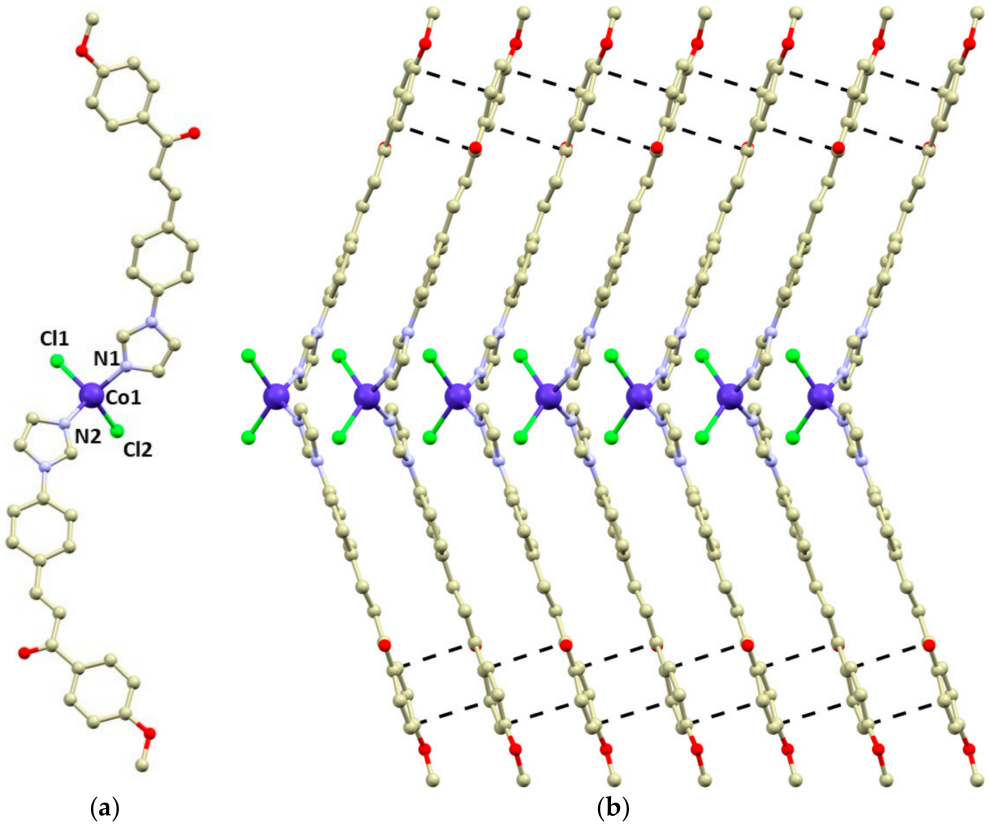

Figure 1. (**a**)—molecular structure of **1**. Selected bond lengths (Å) and angles (deg): *d*(Co1-N1) = 2.014(4), *d*(Co1-N2) = 2.016(4), *d*(Co1-Cl1) = 2.255(2), *d*(Co1-Cl2) = 2.257(2), <(N1-Co1-N2) = 125.7(2), and <(Cl1-Co1-Cl2) = 119.44(6). (**b**)—a perspective view of the packing of the $[Co(4MeO\text{-}L)_2Cl_2]$ molecules in the direction of the crystallographic *b*-axis. Observed π–π stacking interactions were visualized by depicting the shortest C···C distances (black dashed lines). The hydrogen atoms are omitted for clarity.

The crystal packing in **1** is stabilized by a plethora of weak hydrogen bonds such as C-H···Cl and C-H···O. Remarkably, the large aromatic systems of the 4MeO-L ligands form π–π stacking

interactions (the shortest C···C distances range between 3.27 and 3.45 Å), which stabilize the formation of supramolecular chains along the b crystallographic axis (Figure 1b).

2.2. Raman Vibrations

We used CVD graphene (Graphenea, San Sebastian, Spain) on a Si/SiO_2 substrate. Figure 2 shows the substrate Raman spectra that helped us to determine the defects involved in the graphene. The Si/SiO_2 Raman spectrum has a main strong phonon band at 520 cm^{-1} and two medium peaks at 301 cm^{-1} and in the region 946–976 cm^{-1} [48,49]. A spectrum of CVD graphene exhibited the strong peaks D at 1347 cm^{-1}, G at 1595 cm^{-1}, and 2D at 2689 cm^{-1}, with the weaker peaks D′ at 1627 cm^{-1} and D+D′′ at 2462 cm^{-1}. The presence of a strong G peak and weak D′ suggests CVD graphene with defects [50].

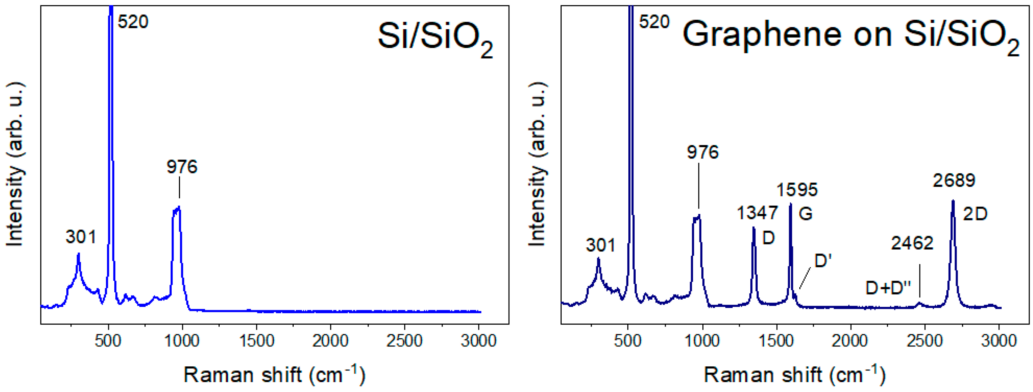

Figure 2. Raman spectra of Si/SiO_2 substrate and graphene on Si/SiO_2 substrate.

A comparison of bulk compound **1**, drop-cast, and two sublimated samples at 75 and 265 °C is illustrated in Figure 3. The Raman spectrum of the bulk compound **1** on the Si/SiO_2 substrate consists of significant peaks (964, 1186, 1366, and 1603 cm^{-1}) and peaks of Si/SiO_2. In the case of the drop-cast sample, significant peaks were overlapped with the peaks of graphene and Si/SiO_2, except one (1190 cm^{-1}). By contrast, the Raman spectra of the sublimated samples all showed significant peaks due to measurements on a larger crystal and obtaining a stronger signal. The comparison tables of the Raman spectra can be found in Table S1.

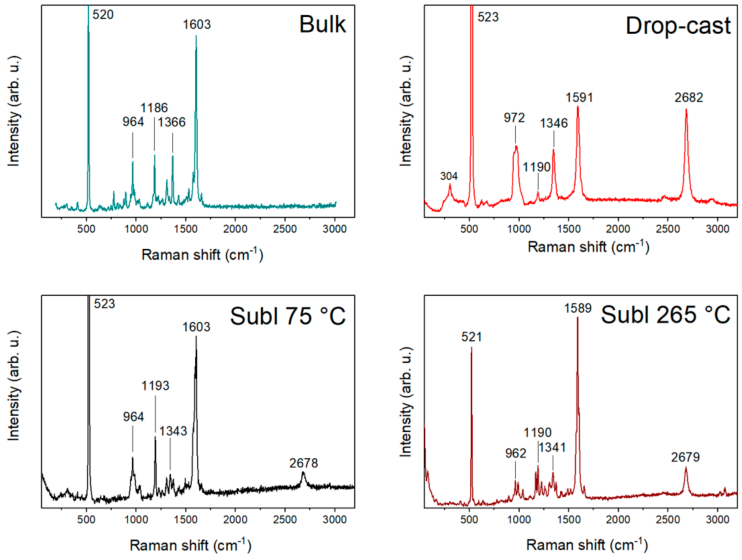

Figure 3. Comparison of Raman spectra of bulk compound **1**, drop-cast, and sublimations at 75 and 265 °C.

Optical images of the hybrid material taken along with Raman spectroscopy are shown in Figure 4. The molecules deposited by drop-casting formed small droplets up to 50 nanometers high. On the contrary, the molecules on sublimated samples formed microcrystals hundreds of nanometers high (see ESI, Figure S1).

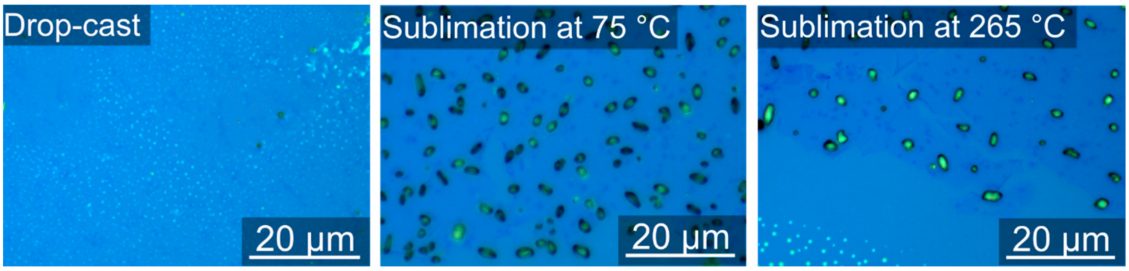

Figure 4. Images from the optical microscope of the samples after drop-casting and sublimations at 75 and 265 °C.

2.3. Chemical Composition and Bonds

The chemical composition was probed by XPS. Figure 5 shows spectra of bulk compound **1** together with the molecular structure.

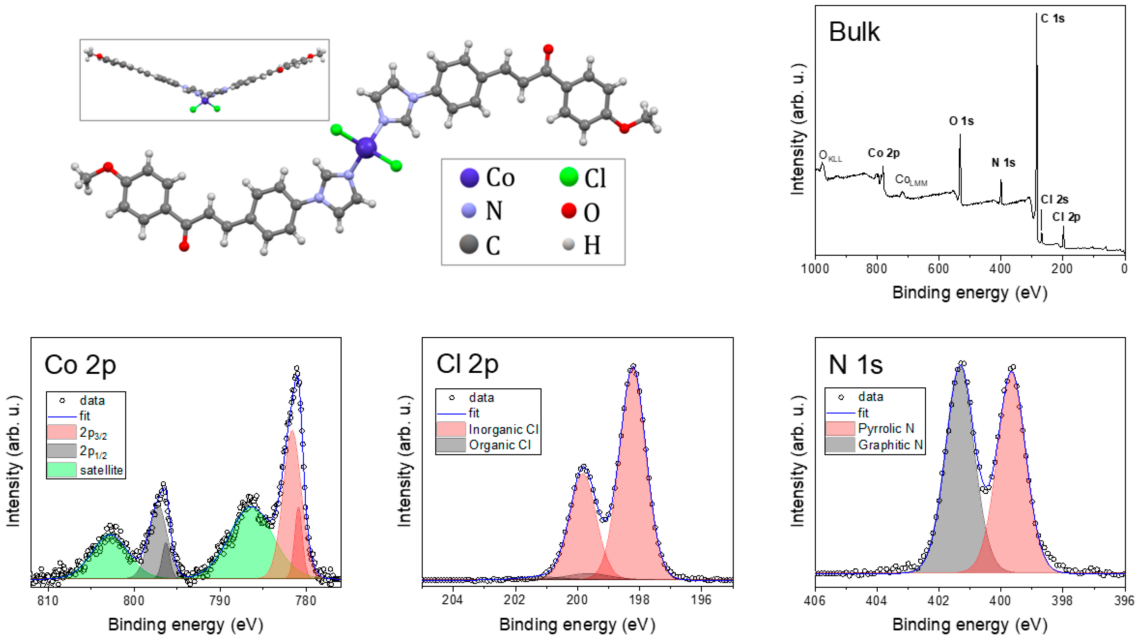

Figure 5. Molecular structure with survey XPS spectrum and detailed Co 2p, Cl 2p, and N 1s spectra.

The bulk compound **1** spectrum exhibited photoelectron peaks—Co 2p, Cl 2p, N 1s, C 1s, and O 1s—and Augers peaks: O_{KLL} and Co_{LMM}. The detailed spectra of the selected peaks revealed specific chemical bonds. The N 1s peak was deconvoluted to two components: graphitic N with three neighboring C atoms and pyrrolic N with two C atoms and one Co bond [51]. The photoelectron peaks emitted from the p, d, and f electronic levels are further split by spin-orbit interactions. This helped us to distinguish, in the Cl 2p spectrum, between organic (Cl–C and Cl–H) and inorganic (Cl–Co) components [52]. Co 2p exhibited two main components and shake-up satellites. The spin-orbit shift of the main components Co $2p_{3/2}$ and Co $2p_{1/2}$ depends on the oxidation state, and with 15.6 eV, the Co(II) high-spin state predominates [53].

Figure 6 shows the comparison of the hybrid samples with CVD graphene: drop-cast, and sublimated at 75 °C and at 265 °C, respectively. In the drop-cast sample, we observed a decrease in

the graphitic nitrogen component compared to bulk compound **1** and an apparent split of chlorine to inorganic and organic contributions. In the case of drop-casting, we detected a weak Co 2p signal on the surface, suggesting a possible complex decomposition (see ESI, Figure S2). In the case of the sublimated samples, even after several hours of acquisition, we did not obtain any convincing Co 2p peaks for 75 or 265 °C. This may be attributed to the possible partial decomposition of the complex or the surface sensitivity of XPS, with the complex outmost layers containing only a very few Co atoms or so-called "dead" layers with oxidized, spoiled molecules. This absence led us to a semi-empirical quantitative analysis of the powder after each sublimation (see ESI, Figure S3) and revealed an increased amount of cobalt and chlorine in the powder from the crucible compared to the bulk powder. This, along with the detected organic chlorine, suggests the possible partial chlorination of the graphene with a partial decomposition of the complex during both deposition processes. Carbon and oxygen contributions were discarded since they might be affected by adventitious contaminations due to the ex situ preparation procedures.

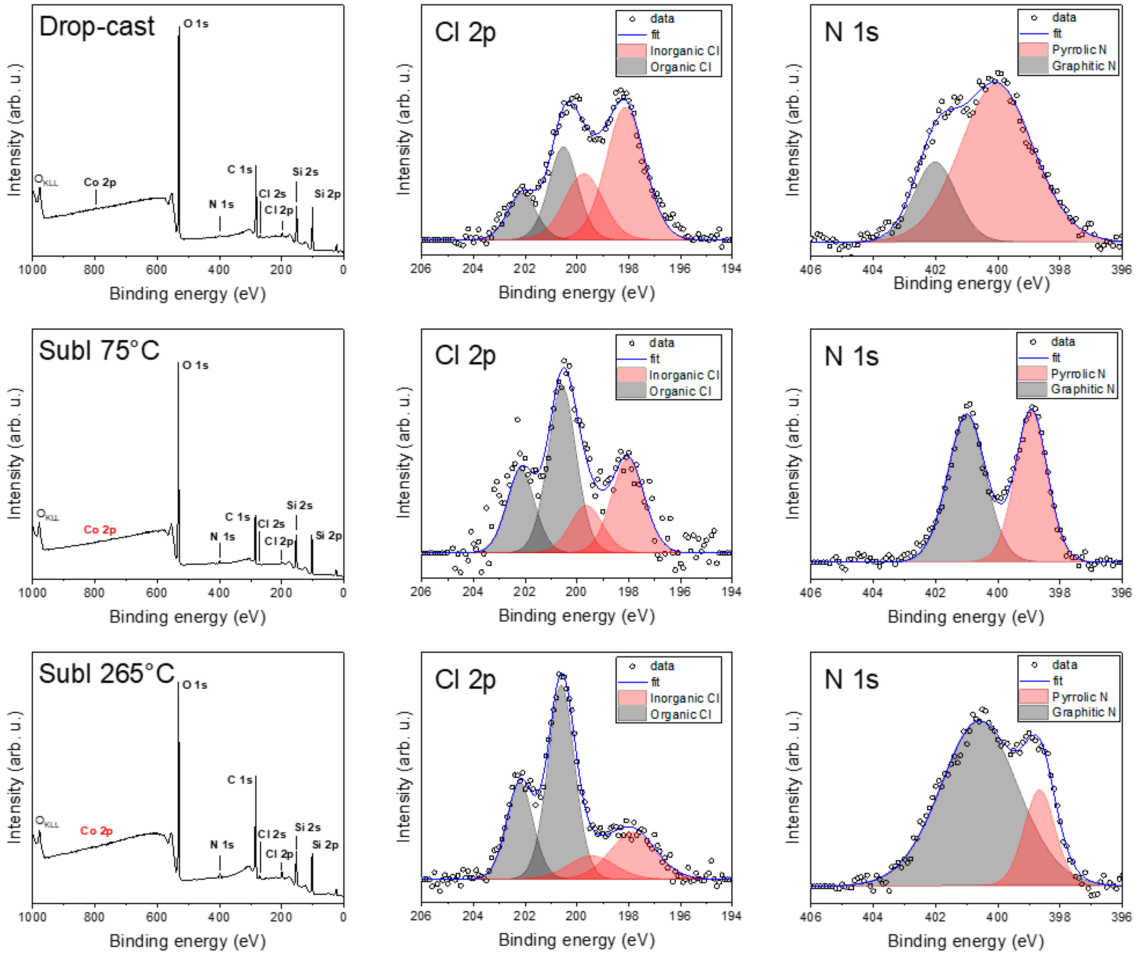

Figure 6. Comparison of detailed XPS spectra of drop-cast and sublimated samples at 75 and 265 °C.

2.4. Molecular Adsorption by DFT

We investigated the adsorption of the molecule on graphene in the framework of density functional theory (DFT) using the Vienna Ab-Initio Simulation Package (VASP) [54–57]. The exchange–correlation potential was approximated by the generalized gradient approximation in Perdew–Burke–Ernzerhof (PBE) parametrization [58,59], the pseudopotential approach was used for the interaction between the valence electrons and ionic core, and Van der Waals forces were considered. Further details can be found in Section 3.

We performed a geometric relaxation calculation considering two possible geometries of the molecule relative to the graphene plane, as shown in Figure 7. The initial position of the molecule was chosen to mimic an AB-stacking configuration between the carbon rings of the molecule and the graphene substrate, as shown in Figure 7b,d, and also to take advantage of possible C–H···π hydrogen bonding between the hydrogen atoms of the molecule and π electrons of the carbon atoms in graphene. The molecule was placed manually on top of the substrate, such that the distances between the closest carbon atom of the molecule and the graphene plane was 3.13 and 3.20 Å for Geometries 1 and 2, respectively. During relaxation, the atoms of the molecule could move freely to their equilibrium positions, while the atoms of the substrate were kept fixed.

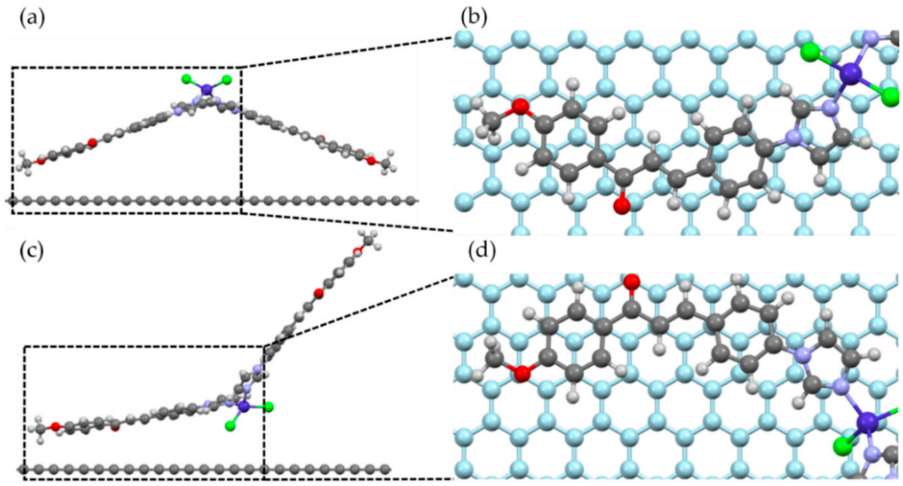

Figure 7. Initial position of the two geometries used for the simulation of molecular adsorption on graphene. As referred to in the text, (**a**) Geometry 1, (**b**) top view of the selected part of (**a**), with the graphene substrate in light blue; the closest carbon atom of the molecule to the substrate was placed in the center of one of the graphene rings. (**c**) Geometry 2, and (**d**) top view of the selected part of (**c**).

After relaxation, we found that the molecule bound to the substrate in both configurations, with distances of 3.31 Å (Geometry 1) and 3.29 Å (Geometry 2) between the closest carbon atom of the molecule and the graphene plane. Such distances correspond to the typical distances between π–π-bonded carbon rings, and we found that there was no considerable change in the molecular shapes after the adsorption. The binding energies were 0.89 eV per molecule (85.4 kJ/mol) for Geometry 1, and 1.08 eV per molecule (104.0 kJ/mol) for Geometry 2, where the main contribution to this energy comes from the van der Waals interactions between the carbon atoms of the molecule and substrate. If van der Waals forces are not considered, the binding energies fall to the meV range, below the thermal energy at room temperature (25.8 meV at 300 K). Therefore, van der Waals forces play a crucial role in the adsorption of these cobalt-based molecules on graphene.

2.5. HF-ESR Spectroscopy

Figure 8 shows the HF-ESR spectra acquired for bulk compound **1** at four frequencies—380, 415, 456, and 490 GHz—while sweeping the magnetic field from 0 to 15 T at 5 K.

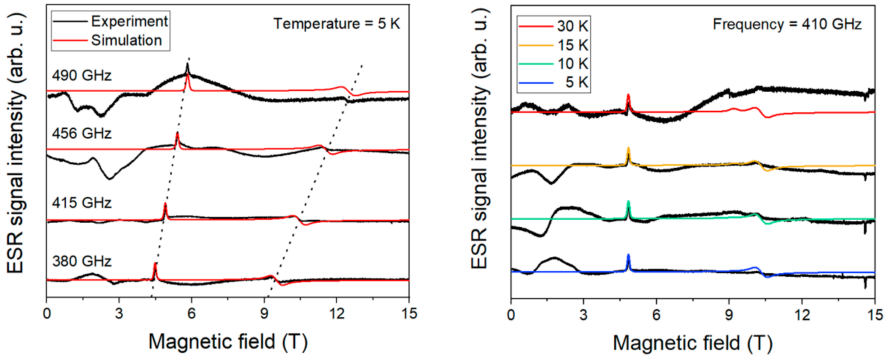

(**a**) (**b**)

Figure 8. (**a**)—high-frequency electron spin resonance (HF-ESR) spectra for four different frequencies at 5 K. The dotted line is guidance for Zeeman splitting. (**b**)—temperature dependence acquired at 410 GHz. Black line in both is experimental, and red/colored line is the simulation.

The used effective spin Hamiltonian for the simulations is the following Equation (1):

$$\hat{H} = \hat{H}_{\text{Zeeman}} + \hat{H}_{\text{ZFS}} = \mu_{\text{B}}\boldsymbol{B}\cdot\boldsymbol{g}\cdot\hat{\boldsymbol{S}} + D\left[\hat{S}_{\text{z}}^2 - \frac{1}{3}S(S+1)\right] + E\left(\hat{S}_{\text{x}}^2 - \hat{S}_{\text{y}}^2\right) \quad (1)$$

where μ_{B} is the Bohr magneton, $\boldsymbol{B}$ is the external magnetic field, $\boldsymbol{g}$ is a tensor linking the external magnetic field with spin vectors, $\hat{\boldsymbol{S}}$ is the electron spin operator, and D and E are axial and rhombic zero-field splitting parameters, respectively. The best fit was found for the spin Hamiltonian parameters as follows: D = 14.6 cm^{-1} with E/D = 0.235, and g_{x} = 2.32, g_{y} = 2.38, and g_{z} = 2.16 (Table 1).

Table 1. Zero-field-splitting (ZFS) parameters obtained by complete active space self-consistent field (CASSCF)/N-electron valence second-order perturbation theory (NEVPT2) calculations compared to HF-ESR.

	D/cm^{-1}	E/D	g_x	g_y	g_z	g_{av}
1	+14.5	0.150	2.325	2.378	2.163	2.289
Geometry 1	+16.4	0.090	2.346	2.364	2.150	2.287
Geometry 2	+17.5	0.132	2.345	2.381	2.143	2.290
HF-ESR	+14.6	0.235	2.320	2.380	2.160	2.287

2.6. CASSCF Calculations

To support the analysis of the HF-ESR spectra of **1**, we performed complete active space self-consistent field (CASSCF) calculations complemented by N-electron valence second-order perturbation theory (NEVPT2) using an ORCA 4.2 computational package [60]. The details of the calculations are explained in Section 3—*Theoretical Methods*. The spin Hamiltonian parameters were extracted by utilizing the effective Hamiltonian theory and we obtained a set of the ZFS parameters—for S = 3/2, D = + 14.5 cm^{-1} and E/D = 0.15—and the anisotropy of the g-tensor components was confirmed (g_{x} = 2.325, g_{y} = 2.378, g_{z} = 2.163, and g_{av} = 2.289). These values are in good agreement with the values obtained by HF-ESR spectroscopy. Next, we performed additional calculations for the optimized Geometries 1 and 2 of the [Co(4MeO-L)$_2$Cl$_2$] molecules deposited on the graphene surface as calculated by periodic DFT. The resulting ZFS parameters are, besides the slightly lower rhombicity, rather similar to those calculated for **1** (all the calculated values are summarized in Table 1). The visualizations of the calculated D-tensor principal axes overlaid over the structures of the complex molecules (Figure 9) underline the similarities among **1** and Geometries 1 and 2. The directions of D_{Z} are practically the same in all the studied molecules. However, the directions of the D_{X} and D_{Y} axes differ among the studied molecules (Figure 9).

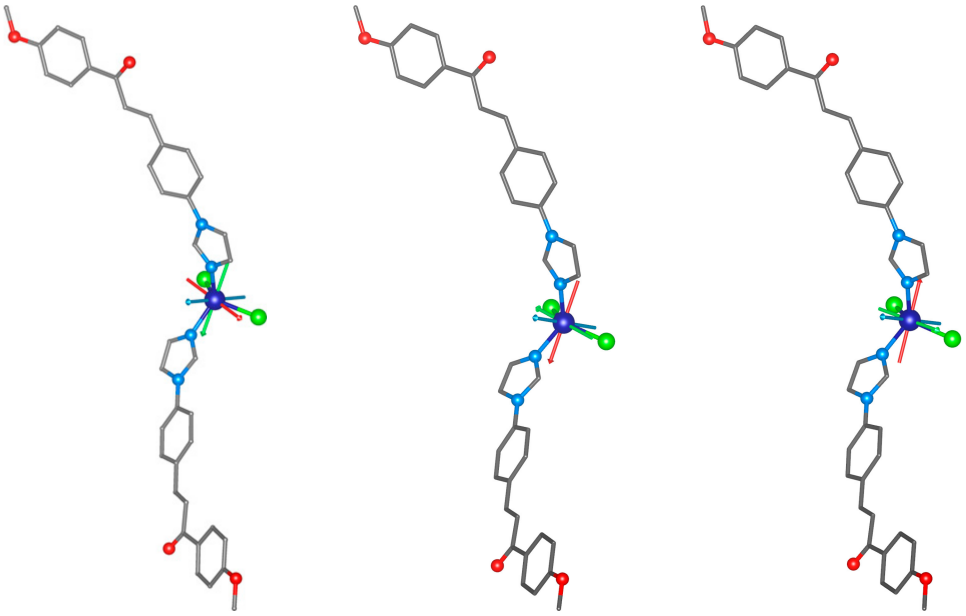

(**a**) (**b**) (**c**)

Figure 9. The CASSCF/NEVPT2 calculated principal axes of the *D*-tensor labeled D_X (red), D_Y (green), and D_Z (blue) visualized together with molecular structures of **1** (**a**), Geometry 1 (**b**), and Geometry 2 (**c**).

3. Materials and Methods

3.1. Materials

$CoCl_2 \cdot 6H_2O$ was bought from PMRLab (Port Elizabeth, South Africa), and 4-(1H-imidazol-1-yl)benzaldehyde, 4-methoxyacetophenone, NaOH, and the solvents (methanol (MeOH), diethyl ether (Et_2O), and the deuterated solvents for the NMR experiments (deuterated chloroform ($CDCl_3$))) were purchased from VWR International (Stříbrná Skalice, Czech Republic), Sigma-Aldrich (Prague, Czech Republic), Lach-Ner (Neratovice, Czech Republic), and Litolab (Chudobín, Czech Republic).

3.2. Synthesis

3.2.1. (2*E*)-3-[4-(1H-imidazol-1-yl)phenyl]-1-(4-methoxyphenyl)prop-2-en-1-one (4MeO-L)

A methanolic sodium hydroxide solution (40%; 1.2 mL) was added dropwise to a mixture of 4-methoxybenzaldehyde (2 mmol, 0.300 g), 4′-(imidazol-1-yl)benzaldehyde (2 mmol, 0.377 g), and methanol (5 mL) over a period of 40 min. The resulting solution was stirred at room temperature until the completion of the reaction. The precipitate was filtered off and washed with a cold methanol–water mixture (1:10). The resulting product was recrystallized from methanol and dried in a desiccator under reduced pressure (overnight) [61].

Yellowish solid. Yield: 83%. ^{1}H NMR (400 MHz, Chloroform-*d*, 298 K, ppm) δ 8.06 (d, *J* = 8.4 Hz, 2H, C17-H, C21-H), 7.92 (s, 1H, C2-H), 7.84–7.74 (m, 3H, C8-H, C10-H, C13-H), 7.57 (d, *J* = 15.6 Hz, 1H, C12-H), 7.46 (d, *J* = 8.1 Hz, 2H, C7-H, C11-H), 7.34 (s, 1H, C5-H), 7.24 (s, 1H, C4-H), 7.00 (d, *J* = 8.4 Hz, 2H, C18-H, C20-H), 3.91 (s, 3H, C23-H). ^{13}C NMR (101 MHz, Chloroform-*d*, 298 K, ppm) δ 188.28 (C14), 163.59 (C19), 142.12 (C12-H), 138.43 (C6), 135.38 (C2-H), 134.23 (C16), 132.72 (C9), 130.87 (C4-H), 130.85 (C8-H, C10-H), 129.86 (C17-H, C21-H), 122.51 (C13-H), 121.45 (C7-H, C11-H), 117.84 (C5-H), 113.91 (C18-H, C20-H), 55.52 (C23-H). ESI+MS (MeOH, *m*/*z*): 305.27 (calc. 305.12; 100%; {4MeO-L + H}$^+$), 327.11 (calc. 327.11; 79%; {4MeO-L + Na}$^+$), 630.81 (calc. 631.67; 88%; {2 × 4MeO-L + Na}$^+$). IR

(ATR, v, cm^{-1}): 407w, 447w, 521w, 593w, 653w, 770w, 816s, 905w, 958w, 981w, 1015m, 1061w, 1120w, 1168m, 1225m, 1254w, 1309w, 1342w, 1433w, 1523s, 1588s, 1658m, 3103w.

3.2.2. Complex $[Co(4MeO\text{-}L)_2(Cl)_2]$ (**1**)

The solution of $CoCl_2{\cdot}6H_2O$ (1 mmol, 0.237 g) in 5 mL of methanol was heated up to 50 °C, and then, 2 molar equiv. of 4MeO-L was added (2 mmol, 0.608 g). The solution was cooled down and stirred at ambient temperature for 2 h. The obtained blue precipitate was collected by filtration and washed with water (2 × 0.5 mL) and Et_2O (2 × 1 mL). The blue solid product was dried in a desiccator under reduced pressure (overnight) [62].

Blue solid. Yield: 92%. Anal. Calc. for $CoC_{38}H_{32}Cl_2N_4O_4$ (**1**): C, 61.80; H, 4.37; N, 7.59%; found: C, 61.59; H, 4.31; N, 7.42%. ESI+MS (MeOH, *m*/*z*,): 305.34 (calc. 305.7; 10%; {4MeO-L + H}$^+$), 471.07 (calc. 471.21; 100%; {[Co(4MeO-L)$(Cl)_2$] + $2H_2O$ + H}$^+$), 702.21 (calc. 702.14; 71%; {[$Co(4MeO\text{-}L)_2(Cl)$]}$^+$), 774.76 (calc. 775.13; 30%; {[$Co(4MeO\text{-}L)_2(Cl)$] + $4H_2O$}$^+$). IR (ATR, v, cm^{-1}): 399w, 412w, 476w, 501w, 517w, 589w, 612w, 646w, 729w, 809s, 969w, 1013w, 1059w, 1102w 1134w, 1159w, 1212w, 1347w, 1401w, 1497w, 1534w, 1598s, 3129w. Thermal stability up to ca. 310 °C was confirmed by thermogravimetry measurement.

3.3. Deposited Samples

Drop-cast sample was prepared by dissolving the bulk compound **1** in dichloromethane (98%, Penta, Czech Republic) to make a final solution with a 100 μM concentration. The actual drop-casting was conducted in a mobile glove bag (Merck, Germany) filled with inert nitrogen gas; 10 μL was drop-cast onto a substrate. For the thermal sublimation, we used a home-built high-vacuum sublimation chamber equipped with a quartz crucible heated by tungsten wire, with a thermocouple in thermal contact with the crucible. The base chamber pressure during the sublimation was 2×10^{-7} mbar. The sublimations were performed at 75 and 265 °C, respectively.

3.4. Raman Spectroscopy (RS)

Raman spectra were acquired on a confocal Raman microscope WITec Alpha300 R+ (WITec, Ulm, Germany). All measurements were carried out with the excitation laser source with a 532 nm wavelength and 1 mW power output. Optical images were acquired with a 100× objective (NA 0.9, WD 0.31 mm).

3.5. Atomic Force Microscopy (AFM)

All topography images and profiles were obtained with the scanning probe microscope Bruker Dimension Icon in tapping mode.

3.6. X-ray Photoelectron Spectroscopy (XPS)

X-ray photoelectron (XPS) measurements were carried out with a Kratos Axis Supra (Kratos Analytical, Manchester, United Kingdom) spectrometer at room temperature and under ultra-high vacuum (UHV) conditions. The instrument was equipped with a monochromatic Al Kα source of 1486.6 eV (15 mA, 15 kV) and a hemispherical analyzer with a hybrid magnetic and electrostatic lens for enhanced electron collection. Survey and detailed XPS spectra were acquired at normal emission with fixed pass energies of 160 and 20 eV, respectively. All spectra were calibrated to the hydrocarbon peak set to 284.8 eV. The Kratos charge neutralizer system was used on all specimens. The inelastic backgrounds in all the spectra were subtracted according to the Shirley method [63]. Data analysis was based on a standard deconvolution method using a mixed Gaussian (G) and Lorentzian (L) line shape (G = 70% and L = 30%, Gaussian–Lorentzian product) for each component in the spectra. The elemental composition of the samples was evaluated using a semi-empirical approach. The integrated intensity of each component was corrected with the photoionization cross-section calculated for each

atom, neglecting the differences in photoelectron escape length as a function of the kinetic energy [64]. The spectra were analyzed using the CasaXPS software (version 2.3.18).

3.7. High-Frequency Electron Spin Resonance (HF-ESR)

HF-ESR spectra were acquired on a newly home-built spectrometer featuring a signal generator (Virginia Diodes, Charlottesville, VA, USA), an amplifier–multiplier chain (Virginia Diodes, Charlottesville, USA), a quasi-optical bridge (Thomas Keating, Billingshurst, UK), and a 16 T solenoid cryomagnet (Cryogenic, London, UK) with heterodyne signal detection. The reference powder sample of the complex was studied as a pressed powder with a ø 5 mm pellet sample. All ESR spectra were simulated using EasySpin [65], a toolbox for Matlab.

3.8. Density Functional Theory (DFT)

The density functional calculations for molecular adsorption were performed with the Vienna Ab-Initio Simulation Package (VASP) [54–57] version 5.4.4, which uses a plane-wave basis for the Kohn–Sham orbitals, the Projector Augmented Wave (PAW) method [57,66], and pseudopotentials. The exchange–correlation potential was approximated by generalized gradient approximation in Perdew–Burke–Ernzerhof (PBE) parametrization [58,59]. Van der Waals corrections were calculated using the D2 method of Grimme [67]. In all calculations, the kinetic energy cut-off for the plane waves was 420 eV. For the calculation of the ground state energy of the system molecule+substrate and graphene substrate, a Γ-centered $2 \times 2 \times 1$ Monkhorst–Pack mesh [68] was used to sample the Brillouin zone, while a Γ-point calculation was used for the ground-state energy of the molecule. We considered two different molecular geometries relative to the graphene plane. Geometry 1 lies on top of a 17×8 graphene supercell, while a 13×7 supercell was used for Geometry 2 (1×1 corresponds to graphene's unit cell). Since a plane-wave basis was used, the systems were periodic along each lattice vector; therefore, an array of infinite molecules was simulated, which in principle can interact with each other. Nevertheless, the distance between the closest atoms of neighboring molecules was no less than 9.0 Å for Geometry 1 and 5.8 Å for Geometry 2 (the distance between the closest Co atoms was 17.2 Å for Geometry 1, and 19.7 Å for Geometry 2); therefore, it was assumed that the molecules did not interact with each other. Geometry relaxation was performed until the forces were below 0.1 eV/Å.

3.9. Theoretical Methods (CASSCF/NEVPT2)

All the theoretical calculations were performed with the ORCA 4.2 computational package [69]. All the calculations employed the triple-ζ def2-TZVP basis functions for all atoms except for carbon and hydrogen, for which the def2-SVP basis set was applied [70]. Additionally, the def2/J and def2-TZVP/C auxiliary basis sets were utilized together with RIJCOSX approximation [71,72]. The multiconfigurational character of the studied Co(II) complexes was handled by calculations utilizing self-consistent field (SA-CASSCF) wave functions [73] with N-electron valence second-order perturbation theory (NEVPT2) [74]. The active space of the CASSCF calculation was set to five d-orbitals of Co(II) (CAS(7,5)). The *D*- and *g*-tensors, based on dominant spin−orbit coupling contributions from excited states, were calculated through quasi-degenerate perturbation theory (QDPT) [75]. We utilized approximations to the Breit–Pauli form of the spin-orbit coupling operator (SOMF approximation) [76] and effective Hamiltonian theory [77].

3.10. Elemental Analyses (EA)

Elemental analysis was carried out using a Flash 2000 CHNS Elemental Analyzer (Thermo Scientific, Waltham, MA, USA).

3.11. Mass Spectrometry (MS)

Electrospray ionization mass spectrometry (ESI-MS; methanol solutions) was performed with an LCQ Fleet ion trap spectrometer (Thermo Scientific, Waltham, MA, USA; QualBrowser software, version 2.0.7) in both positive (ESI+) and negative (ESI-) ionization modes.

3.12. NMR Spectroscopy

^{1}H and ^{13}C NMR spectroscopy, and ^{1}H-^{13}C gsHMQC and ^{1}H-^{13}C gsHMBC two-dimensional correlation experiments were performed using $CDCl_3$ (4MeO-L) solution at 300 K using a Varian spectrometer (Palo Alto, CA, USA) at 400.00 MHz (for ^{1}H NMR) and 101.00 MHz (for ^{13}C NMR), where gs = the gradient selected, HMQC = the heteronuclear multiple quantum coherence, and HMBC = the heteronuclear multiple bond coherence. ^{1}H and ^{13}C NMR spectra were calibrated against the residual $CDCl_3$ ^{1}H NMR (7.26 ppm) and ^{13}C NMR (77.16 ppm) signals. The splitting of the proton resonances in the reported ^{1}H spectra is defined as s = singlet, d = doublet, dd = doublet of doublets, sep = septet, m = multiplet, and bs = broad signal.

3.13. Infrared Spectroscopy

A Jasco FT/IR-4700 spectrometer (Jasco, Easton, MD, USA) was used for the collection of the infrared (IR) spectra of the studied ligand and complex in the range of 400–4000 cm^{-1} by using the attenuated total reflection (ATR) technique on a diamond plate.

3.14. Crystallography

A single crystal of **1** was mounted on a Stoe StadiVari diffractometer possessing a Pilatus3R 300 K detector and microfocused sealed tube Xenocs Genix3D Cu HF (λ = 1.54186 Å) at 100 K. The structure was solved using the program SuperFlip [78] and refined using the program ShelXL (ver. 2018/3) [79] in the crystallographic package Olex2 [80]. The structure was drawn using the Mercury program [81]. Crystal data for $CoC_{38}H_{32}Cl_2N_4O_4$ (M = 738.50 g/mol): monoclinic, space group *Pc* (no. 7), a = 18.7700(3) Å, b = 12.2910(4) Å, c = 7.3969(6) Å, β = 101.392(3)°, V = 1672.86(15) Å^3, Z = 2, T = 100(1) K, μ(CuKα) = 5.885 mm^{-1}, D_{calc} = 1.466 g/cm^3, 31,686 reflections measured (3.596° ≤ 2Θ ≤ 72.338°), 5367 unique (R_{int} = 0.0372), used in all calculations. The final R1 was 0.0455 (I > 2σ(I)), and the wR_2 was 0.1211 (all data). The highest peak: +0.28; the deepest hole: −0.53. Crystal structure refinement: All atoms except for hydrogen were refined anisotropically. The hydrogen atoms were placed into the calculated positions, and they were included into the riding-model approximation with U_{iso} = 1.2U_{eq}(C) or 1.5 U_{eq} (CH_3) and d(C−H) = 0.95–0.98 Å.

4. Conclusions

This paper reports on the synthesis, crystal structure, magnetic properties, and characterization of a new Co(II)-based complex with monodentate chalcone ligands and its deposition on graphene. The magnetic properties were determined from HF-ESR measurements and were found to be in fair agreement with CASSCF/NEVPT2 ab initio quantum chemical calculations. The spin Hamiltonian parameters are as follows: D = 14.6 cm^{-1} with significant rhombicity E/D = 0.235, and g_x = 2.32, g_y = 2.38, and g_z = 2.16. Depositions on graphene were attempted by both drop-casting in an inert nitrogen atmosphere and by the thermal sublimation of bulk compound **1** in a high vacuum. In both cases, we observed organic chlorine components, suggesting the partial decomposition of the complex or possible chlorination of graphene. On the contrary, the Raman spectra showed a good agreement of the peaks in bulk and on the graphene; however, a few peaks from the complex overlapped with the graphene peaks, which hindered the analysis. In the case of the drop-cast sample, we observed the formation of small nanodroplets about 50 nm high on the graphene. Samples prepared by thermal sublimations revealed the formation of microcrystallites formed mostly at the grain edges and defects on graphene. DFT simulations of the complex at two geometries on the graphene surface confirmed only weak

attraction to the graphene surface, with the crucial role of van der Waals forces in the adsorption on graphene. The outlook for the successful deposition of intact complexes on graphene surfaces requires the fine chemical tailoring of ligands, promoting adhesion on graphene, and utilizing chelation agents that protect the complex from detrimental effects such as atmospheric moisture, oxidation, and thermal decomposition. The next step after successful deposition is to obtain the magnetic properties of a thin film on the surface, which will be obtained from HF-ESR measurements or from X-ray magnetic circular dichroism (XMCD) at the synchrotron facility.

Supplementary Materials: The following are available online. Table S1: Comparison of Raman shift peaks (in cm−1) for drop-casting. Peak intensity is denoted as follows: strong—s, medium—m, and weak—w. Figure S1: AFM images from drop-cast and sublimated samples at 75 and 265 °C. Figure S2: Weak Co 2p peak from the drop-cast sample. Figure S3: Elemental percentage of atoms in powder from crucible after thermal sublimation at 75 and 265 °C. Deposition Number 2034425 (1) contains the supplementary crystallographic data for this paper.

Author Contributions: XPS, depositions, and writing—original manuscript, J.H.; AFM, Raman, and depositions, Š.V.; chemical synthesis and analytical characterization of ligand and complex, L.M.; HF-ESR experiments, A.S.; DFT calculations, J.N.-G.; graphene sample preparation, M.B.; CASSCF/NEVPT2, R.H.; crystal structure measurements, J.M.; XRD analysis and writing, I.N.; supervision, P.N. All authors have read and agreed to the published version of the manuscript.

Funding: This research was funded by the Ministry of Education, Youth and Sports of the Czech Republic: grant number CEITEC 2020 (LQ1601); LTAUSA19060 in the INTER-EXCELLENCE Programme; GAČR 19-01536S; the ERC under the European Union's Horizon 2020 Research and Innovation Programme (GA No. 714850); and an internal grant of Brno University of Technology CEITEC-VUT-J-20-6514, J.N.-G. is a holder of the Brno Ph.D. Talent Scholarship—Funded by the Brno City Municipality. R.H., I.N., and L.M. acknowledge financial support from the Palacký University Olomouc project IGA_PrF_2020_016. J.M. acknowledges financial support for the structural analysis from the Grant Agencies of the Slovak Republic (VEGA 1/0639/18, APVV-19-0087).

Acknowledgments: J.H. acknowledges Tomáš Kralevic Musálek and Radek Řihák (Activair, Czech Republic) for help with the design and manufacture of the custom UHV sublimation chamber. J.N.-G. acknowledges Davonne Henry and Amy Liu (Georgetown University, USA) for a fruitful discussion and support with DFT on surfaces.

Conflicts of Interest: The authors declare no conflict of interest.

References

1. Caneschi, A.; Gatteschi, D.; Sessoli, R.; Barra, A.L.; Brunei, L.C.; Guillot, M. Alternating Current Susceptibility, High Field Magnetization, and Millimeter Band EPR Evidence for a Ground S=10 State in [Mn12O12(CH3COO)16(H2O)4].2CH3COOH.4H2O. *J. Am. Chem. Soc.* **1991**, *113*, 5873–5874. [CrossRef]
2. Sessoli, R.; Gatteschi, D.; Tsai, H.L.; Hendrickson, D.N.; Schake, A.R.; Wang, S.; Vincent, J.B.; Christou, G.; Folting, K. High-Spin Molecules: [Mn12O12(O2CR)16(H2O)4]. *J. Am. Chem. Soc.* **1993**, *115*, 1804–1816. [CrossRef]
3. Sessoli, R.; Gatteschi, D.; Caneschi, A.; Novak, M.A. Magnetic bistability in a metal-ion cluster. *Nature* **1993**, *365*, 141–143. [CrossRef]
4. Gatteschi, D.; Sessoli, R.; Villain, J. *Molecular Nanomagnets*, 1st ed.; Oxford University Press: Oxford, UK, 2007; ISBN 9780198567530.
5. Neese, F.; Pantazis, D.A. What is not required to make a single molecule magnet. *Faraday Discuss.* **2011**, *148*, 229–238. [CrossRef]
6. Ishikawa, N.; Sugita, M.; Ishikawa, T.; Koshihara, S.Y.; Kaizu, Y. Lanthanide double-decker complexes functioning as magnets at the single-molecular level. *J. Am. Chem. Soc.* **2003**, *125*, 8694–8695. [CrossRef]
7. Guo, F.-S.; Day, B.M.; Chen, Y.-C.; Tong, M.-L.; Mansikkamäki, A.; Layfield, R.A. Magnetic hysteresis up to 80 kelvin in a dysprosium metallocene single-molecule magnet. *Science* **2018**, *362*, 1400–1403. [CrossRef]
8. Wolf, S.A. Spintronics: A Spin-Based Electronics Vision for the Future. *Science* **2001**, *294*, 1488–1495. [CrossRef] [PubMed]
9. Leuenberger, M.N.; Loss, D. Quantum computing in molecular magnets. *Nature* **2001**, *410*, 789–793. [CrossRef]
10. Bogani, L.; Wernsdorfer, W. Molecular spintronics using single-molecule magnets. *Nat. Mater.* **2008**, *7*, 179–186. [CrossRef]

11. Barra, A.L.; Gatteschi, D.; Sessoli, R. High-frequency EPR spectra of a molecular nanomagnet: Understanding quantum tunneling of the magnetization. *Phys. Rev. B Condens. Matter Mater. Phys.* **1997**, *56*, 8192–8198. [CrossRef]
12. Barra, A.L.; Gatteschi, D.; Sessoli, R. High-frequency EPR spectra of [Fe8O2(OH)12(taCn)6]Br8: A critical appraisal of the barrier for the reorientation of the magnetization in single-molecule magnets. *Chem. Eur. J.* **2000**, *6*, 1608–1614. [CrossRef]
13. Barra, A.L. High-frequency EPR spectroscopy of single-molecule magnets: A case study. *Appl. Magn. Reson.* **2001**, *21*, 619–628. [CrossRef]
14. Krzystek, J.; Ozarowski, A.; Zvyagin, S.A.; Telser, J. High spin Co(I): High-frequency and -field EPR spectroscopy of CoX(PPh 3) 3 (X = Cl, Br). *Inorg. Chem.* **2012**, *51*, 4954–4964. [CrossRef] [PubMed]
15. Rechkemmer, Y.; Fischer, J.E.; Marx, R.; Dörfel, M.; Neugebauer, P.; Horvath, S.; Gysler, M.; Brock-Nannestad, T.; Frey, W.; Reid, M.F.; et al. Comprehensive Spectroscopic Determination of the Crystal Field Splitting in an Erbium Single-Ion Magnet. *J. Am. Chem. Soc.* **2015**, *137*, 13114–13120. [CrossRef]
16. Realista, S.; Fitzpatrick, A.J.; Santos, G.; Ferreira, L.P.; Barroso, S.; Pereira, L.C.J.; Bandeira, N.A.G.; Neugebauer, P.; Hrubý, J.; Morgan, G.G.; et al. A Mn(III) single ion magnet with tridentate Schiff-base ligands. *Dalton Trans.* **2016**, *45*, 12301–12307. [CrossRef]
17. Kultaeva, A.; Biktagirov, T.; Neugebauer, P.; Bamberger, H.; Bergmann, J.; Van Slageren, J.; Krautscheid, H.; Pöppl, A. Multifrequency EPR, SQUID, and DFT Study of Cupric Ions and Their Magnetic Coupling in the Metal-Organic Framework Compound ∞3[Cu(prz-trz-ia)]. *J. Phys. Chem. C* **2018**, *122*, 26642–26651. [CrossRef]
18. Neugebauer, P.; Bloos, D.; Marx, R.; Lutz, P.; Kern, M.; Aguilà, D.; Vaverka, J.; Laguta, O.; Dietrich, C.; Clérac, R.; et al. Ultra-broadband EPR spectroscopy in field and frequency domains. *Phys. Chem. Chem. Phys.* **2018**, *20*, 15528–15534. [CrossRef]
19. Bucinsky, L.; Breza, M.; Malček, M.; Powers, D.C.; Hwang, S.J.; Krzystek, J.; Nocera, D.G.; Telser, J. High-Frequency and -Field EPR (HFEPR) Investigation of a Pseudotetrahedral Cr IV Siloxide Complex and Computational Studies of Related Cr IV L 4 Systems. *Inorg. Chem.* **2019**, *58*, 4907–4920. [CrossRef]
20. Hrubý, J.; Dvořák, D.; Squillantini, L.; Mannini, M.; van Slageren, J.; Herchel, R.; Nemec, I.; Neugebauer, P. Co(ii)-Based single-ion magnets with 1,1′-ferrocenediyl-bis(diphenylphosphine) metalloligands. *Dalton Trans.* **2020**, *2*, 11697–11707. [CrossRef]
21. Hrubý, J.; Santana, V.T.; Kostiuk, D.; Bouček, M.; Lenz, S.; Kern, M.; Šiffalovič, P.; van Slageren, J.; Neugebauer, P. A graphene-based hybrid material with quantum bits prepared by the double Langmuir–Schaefer method. *RSC Adv.* **2019**, *9*, 24066–24073. [CrossRef]
22. Marie, L.S.; El Fatimy, A.; Hrubý, J.; Nemec, I.; Hunt, J.; Myers-Ward, R.; Gaskill, D.K.; Kruskopf, M.; Yang, Y.; Elmquist, R.; et al. Nanostructured graphene for nanoscale electron paramagnetic resonance spectroscopy. *J. Phys. Mater.* **2020**, *3*, 014013. [CrossRef]
23. Ciccullo, F.; Glaser, M.; Sättele, M.S.; Lenz, S.; Neugebauer, P.; Rechkemmer, Y.; Van Slageren, J.; Casu, M.B. Thin film properties and stability of a potential molecular quantum bit based on copper(ii). *J. Mater. Chem. C* **2018**, *6*, 8028–8034. [CrossRef]
24. Holmberg, R.J.; Murugesu, M. Adhering magnetic molecules to surfaces. *J. Mater. Chem. C* **2015**, *3*, 11986–11998. [CrossRef]
25. Caneschi, A.; Gatteschi, D.; Totti, F. Molecular magnets and surfaces: A promising marriage. A DFT insight. *Coord. Chem. Rev.* **2015**, *289–290*, 357–378. [CrossRef]
26. Mannini, M.; Pineider, F.; Sainctavit, P.; Danieli, C.; Otero, E.; Sciancalepore, C.; Talarico, A.M.; Arrio, M.A.; Cornia, A.; Gatteschi, D.; et al. Magnetic memory of a single-molecule quantum magnet wired to a gold surface. *Nat. Mater.* **2009**, *8*, 194–197. [CrossRef]
27. Saywell, A.; Magnano, G.; Satterley, C.J.; Perdigão, L.M.A.; Britton, A.J.; Taleb, N.; Del Carmen Giménez-López, M.; Champness, N.R.; O'Shea, J.N.; Beton, P.H. Self-assembled aggregates formed by single-molecule magnets on a gold surface. *Nat. Commun.* **2010**, *1*, 75. [CrossRef]
28. Rozbořil, J.; Rechkemmer, Y.; Bloos, D.; Münz, F.; Wang, C.N.; Neugebauer, P.; Čechal, J.; Novák, J.; van Slageren, J. Magneto-optical investigations of molecular nanomagnet monolayers. *Dalton Trans.* **2016**, *45*, 7555–7558. [CrossRef]

29. Malavolti, L.; Lanzilotto, V.; Ninova, S.; Poggini, L.; Cimatti, I.; Cortigiani, B.; Margheriti, L.; Chiappe, D.; Otero, E.; Sainctavit, P.; et al. Magnetic bistability in a submonolayer of sublimated Fe4 single-molecule magnets. *Nano Lett.* **2015**, *15*, 535–541. [CrossRef]
30. Kiefl, E.; Mannini, M.; Bernot, K.; Yi, X.; Amato, A.; Leviant, T.; Magnani, A.; Prokscha, T.; Suter, A.; Sessoli, R.; et al. Robust Magnetic Properties of a Sublimable Single-Molecule Magnet. *ACS Nano* **2016**, *10*, 5663–5669. [CrossRef]
31. Lanzilotto, V.; Malavolti, L.; Ninova, S.; Cimatti, I.; Poggini, L.; Cortigiani, B.; Mannini, M.; Totti, F.; Cornia, A.; Sessoli, R. The Challenge of Thermal Deposition of Coordination Compounds: Insight into the Case of an Fe4 Single Molecule Magnet. *Chem. Mater.* **2016**, *28*, 7693–7702. [CrossRef]
32. Cañon-Mancisidor, W.; Miralles, S.G.; Baldoví, J.J.; Espallargas, G.M.; Gaita-Ariño, A.; Coronado, E. Sublimable Single Ion Magnets Based on Lanthanoid Quinolinate Complexes: The Role of Intermolecular Interactions on Their Thermal Stability. *Inorg. Chem.* **2018**, *57*, 14170–14177. [CrossRef]
33. Miralles, S.G.; Bedoya-Pinto, A.; Baldoví, J.J.; Cañon-Mancisidor, W.; Prado, Y.; Prima-Garcia, H.; Gaita-Ariño, A.; Mínguez Espallargas, G.; Hueso, L.E.; Coronado, E. Sublimable chloroquinolinate lanthanoid single-ion magnets deposited on ferromagnetic electrodes. *Chem. Sci.* **2018**, *9*, 199–208. [CrossRef]
34. Margheriti, L.; Mannini, M.; Sorace, L.; Gorini, L.; Gatteschi, D.; Caneschi, A.; Chiappe, D.; Moroni, R.; de Mongeot, F.B.; Cornia, A.; et al. Thermal Deposition of Intact Tetrairon(III) Single-Molecule Magnets in High-Vacuum Conditions. *Small* **2009**, *5*, 1460–1466. [CrossRef]
35. Geim, A.K.; Novoselov, K.S. The rise of graphene. *Nat. Mater.* **2007**, *6*, 183–191. [CrossRef]
36. Du, X.; Skachko, I.; Andrei, E.Y.; Barker, A. Approaching ballistic transport in suspended graphene. *Nat. Nanotechnol.* **2008**, *3*, 491–495. [CrossRef]
37. Neugebauer, P.; Orlita, M.; Faugeras, C.; Barra, A.L.; Potemski, M. How perfect can graphene be? *Phys. Rev. Lett.* **2009**, *103*, 136403. [CrossRef]
38. Lee, C.; Wei, X.; Kysar, J.W.; Hone, J. Measurement of the Elastic of Properties and Intrinsic Strength of Monolayer Graphene. *Science* **2008**, *321*, 385–388. [CrossRef]
39. Seol, J.H.; Jo, I.; Moore, A.L.; Lindsay, L.; Aitken, Z.H.; Pettes, M.T.; Li, X.; Yao, Z.; Huang, R.; Broido, D.; et al. Two-dimensional phonon transport in supported graphene. *Science* **2010**, *328*, 213–216. [CrossRef]
40. Novoselov, K.S.S.; Geim, A.K.K.; Morozov, S.V.V.; Jiang, D.; Zhang, Y.; Dubonos, S.V.V.; Grigorieva, I.V.V.; Firsov, A.A.A. Electric Field Effect in Atomically Thin Carbon Films. *Science* **2004**, *306*, 666–669. [CrossRef]
41. Warner, J.H.; Mukai, M.; Kirkland, A.I. Atomic structure of ABC rhombohedral stacked trilayer graphene. *ACS Nano* **2012**, *6*, 5680–5686. [CrossRef]
42. VanMil, B.L.; Myers-Ward, R.L.; Tedesco, J.L.; Eddy, C.R., Jr.; Jernigan, G.G.; Culbertson, J.C.; Campbell, P.M.; McCrate, J.M.; Kitt, S.A.; Gaskill, D.K. Graphene Formation on SiC Substrates. *Mater. Sci. Forum* **2009**, *615–617*, 211–214. [CrossRef]
43. Coleman, J.N.; Lotya, M.; O'Neill, A.; Bergin, S.D.; King, P.J.; Khan, U.; Young, K.; Gaucher, A.; De, S.; Smith, R.J.; et al. Two-dimensional nanosheets produced by liquid exfoliation of layered materials. *Science* **2011**, *331*, 568–571. [CrossRef] [PubMed]
44. Bae, S.; Kim, H.; Lee, Y.; Xu, X.; Park, J.S.; Zheng, Y.; Balakrishnan, J.; Lei, T.; Ri Kim, H.; Song, Y.; et al. Roll-to-roll production of 30-inch graphene films for transparent electrodes. *Nat. Nanotechnol.* **2010**, *5*, 574–578. [CrossRef] [PubMed]
45. Atanasov, M.; Aravena, D.; Suturina, E.; Bill, E.; Maganas, D.; Neese, F. First principles approach to the electronic structure, magnetic anisotropy and spin relaxation in mononuclear 3d-transition metal single molecule magnets. *Coord. Chem. Rev.* **2015**, *289–290*, 177–214. [CrossRef]
46. *SHAPE, Version 2.1*; University of Barcelona: Barcelona, Spain, 2013.
47. Alvarez, S. Polyhedra in (inorganic) chemistry. *Dalton Trans.* **2005**, *13*, 2209–2233. [CrossRef]
48. Mankad, V.; Gupta, S.K.; Jha, P.K.; Ovsyuk, N.N.; Kachurin, G.A. Low-frequency Raman scattering from Si/Ge nanocrystals in different matrixes caused by acoustic phonon quantization. *J. Appl. Phys.* **2012**, *112*, 54318. [CrossRef]
49. Spizzirri, P.G.; Fang, J.H.; Rubanov, S.; Gauja, E.; Prawer, S. Nano-Raman spectroscopy of silicon surfaces. *arXiv* **2010**, arXiv:1002.2692.
50. Ferrari, A.C. Raman spectroscopy of graphene and graphite: Disorder, electron-phonon coupling, doping and nonadiabatic effects. *Solid State Commun.* **2007**, *143*, 47–57. [CrossRef]

51. Akula, S.; Parthiban, V.; Peera, S.G.; Singh, B.P.; Dhakate, S.R.; Sahu, A.K. Simultaneous Co-Doping of Nitrogen and Fluorine into MWCNTs: An In-Situ Conversion to Graphene Like Sheets and Its Electro-Catalytic Activity toward Oxygen Reduction Reaction. *J. Electrochem. Soc.* **2017**, *164*, F568–F576. [CrossRef]
52. Fiedler, R.; Herzschuh, R. An XPS investigation of the effects of heat treatment on the chlorine surface chemistry of some lignites. *Fuel* **1993**, *72*, 1501–1505. [CrossRef]
53. Poneti, G.; Mannini, M.; Cortigiani, B.; Poggini, L.; Sorace, L.; Otero, E.; Sainctavit, P.; Sessoli, R.; Dei, A. Magnetic and spectroscopic investigation of thermally and optically driven valence tautomerism in thioether-bridged dinuclear cobalt-dioxolene complexes. *Inorg. Chem.* **2013**, *52*, 11798–11805. [CrossRef]
54. Kresse, G.; Hafner, J. Ab initio molecular dynamics for liquid metals. *Phys. Rev. B* **1993**, *47*, 558–561. [CrossRef]
55. Kresse, G.; Furthmüller, J. Efficiency of ab-initio total energy calculations for metals and semiconductors using a plane-wave basis set. *Comput. Mater. Sci.* **1996**, *6*, 15–50. [CrossRef]
56. Kresse, G.; Furthmüller, J. Efficient iterative schemes for ab initio total-energy calculations using a plane-wave basis set. *Phys. Rev. B Condens. Matter Mater. Phys.* **1996**, *54*, 11169–11186. [CrossRef] [PubMed]
57. Kresse, G.; Joubert, D. From ultrasoft pseudopotentials to the projector augmented-wave method. *Phys. Rev. B* **1999**, *59*, 1758–1775. [CrossRef]
58. Perdew, J.P.; Burke, K.; Ernzerhof, M. Generalized Gradient Approximation Made Simple. *Phys. Rev. Lett.* **1996**, *77*, 3865–3868. [CrossRef]
59. Perdew, J.P.; Burke, K.; Ernzerhof, M. Generalized Gradient Approximation Made Simple [Phys. Rev. Lett. 77, 3865 (1996)]. *Phys. Rev. Lett.* **1997**, *78*, 1396. [CrossRef]
60. Neese, F. The ORCA program system. *Wiley Interdiscip. Rev. Comput. Mol. Sci.* **2012**, *2*, 73–78. [CrossRef]
61. Hussain, T.; Siddiqui, H.L.; Zia-ur-Rehman, M.; Masoom Yasinzai, M.; Parvez, M. Anti-oxidant, anti-fungal and anti-leishmanial activities of novel 3-[4-(1H-imidazol-1-yl) phenyl]prop-2-en-1-ones. *Eur. J. Med. Chem.* **2009**, *44*, 4654–4660. [CrossRef]
62. Masaryk, L.; Moncol, J.; Herchel, R.; Nemec, I. Halogen Bonding in New Dichloride-Cobalt(II) Complex with Iodo Substituted Chalcone Ligands. *Crystals* **2020**, *10*, 354. [CrossRef]
63. Shirley, D.A. High-resolution x-ray photoemission spectrum of the valence bands of gold. *Phys. Rev. B* **1972**, *5*, 4709–4714. [CrossRef]
64. Yeh, J.J.; Lindau, I. Atomic subshell photoionization cross sections and asymmetry parameters: $1 \leq Z \leq 103$. *At. Data Nucl. Data Tables* **1985**, *32*, 1–155. [CrossRef]
65. Stoll, S.; Schweiger, A. EasySpin, a comprehensive software package for spectral simulation and analysis in EPR. *J. Magn. Reson.* **2006**, *178*, 42–55. [CrossRef]
66. Blöchl, P.E. Projector augmented-wave method. *Phys. Rev. B* **1994**, *50*, 17953–17979. [CrossRef] [PubMed]
67. Grimme, S. Semiempirical GGA-type density functional constructed with a long-range dispersion correction. *J. Comput. Chem.* **2006**, *27*, 1787–1799. [CrossRef]
68. Monkhorst, H.J.; Pack, J.D. Special points for Brillouin-zone integrations. *Phys. Rev. B* **1976**, *13*, 5188–5192. [CrossRef]
69. Neese, F. Software update: The ORCA program system, version 4.0. *Wiley Interdiscip. Rev. Comput. Mol. Sci.* **2018**, *8*, e1327. [CrossRef]
70. Weigend, F.; Ahlrichs, R. Balanced basis sets of split valence, triple zeta valence and quadruple zeta valence quality for H to Rn: Design and assessment of accuracy. *Phys. Chem. Chem. Phys.* **2005**, *7*, 3297–3305. [CrossRef]
71. Weigend, F. Accurate Coulomb-fitting basis sets for H to Rn. *Phys. Chem. Chem. Phys.* **2006**, *8*, 1057–1065. [CrossRef]
72. Hellweg, A.; Hättig, C.; Höfener, S.; Klopper, W. Optimized accurate auxiliary basis sets for RI-MP2 and RI-CC2 calculations for the atoms Rb to Rn. *Theor. Chem. Acc.* **2007**, *117*, 587–597. [CrossRef]
73. Malmqvist, P.Å.; Roos, B.O. The CASSCF state interaction method. *Chem. Phys. Lett.* **1989**, *155*, 189–194. [CrossRef]
74. Angeli, C.; Cimiraglia, R.; Evangelisti, S.; Leininger, T.; Malrieu, J.P. Introduction of n-electron valence states for multireference perturbation theory. *J. Chem. Phys.* **2001**, *114*, 10252. [CrossRef]
75. Ganyushin, D.; Neese, F. First-principles calculations of zero-field splitting parameters. *J. Chem. Phys.* **2006**, *125*, 024103. [CrossRef] [PubMed]

76. Neese, F. Efficient and accurate approximations to the molecular spin-orbit coupling operator and their use in molecular g-tensor calculations. *J. Chem. Phys.* **2005**, *122*, 034107. [CrossRef] [PubMed]
77. Maurice, R.; Bastardis, R.; de Graaf, C.; Suaud, N.; Mallah, T.; Guihéry, N. Universal theoretical approach to extract anisotropic spin hamiltonians. *J. Chem. Theory Comput.* **2009**, *5*, 2977–2984. [CrossRef]
78. Palatinus, L.; Chapuis, G. SUPERFLIP—A computer program for the solution of crystal structures by charge flipping in arbitrary dimensions. *J. Appl. Crystallogr.* **2007**, *40*, 786–790. [CrossRef]
79. Sheldrick, G.M. Crystal structure refinement with SHELXL. *Acta Crystallogr. Sect. C Struct. Chem.* **2015**, *71*, 3–8. [CrossRef]
80. Dolomanov, O.V.; Bourhis, L.J.; Gildea, R.J.; Howard, J.A.K.; Puschmann, H. OLEX2: A complete structure solution, refinement and analysis program. *J. Appl. Crystallogr.* **2009**, *42*, 339–341. [CrossRef]
81. MacRae, C.F.; Sovago, I.; Cottrell, S.J.; Galek, P.T.A.; McCabe, P.; Pidcock, E.; Platings, M.; Shields, G.P.; Stevens, J.S.; Towler, M.; et al. Mercury 4.0: From visualization to analysis, design and prediction. *J. Appl. Crystallogr.* **2020**, *53*, 226–235. [CrossRef]

Sample Availability: Samples are available from the authors upon request in limited amount.